Flow Turbulence Combust (2016) 97:1211–1233
DOI 10.1007/s10494-016-9774-x

Reconstruction of Scalar Source Intensity Based on Sensor Signal in Turbulent Channel Flow

D. Cerizza[1] · W. Sekiguchi[2] · T. Tsukahara[3] · T. A. Zaki[4] · Y. Hasegawa[1]

Received: 14 January 2016 / Accepted: 14 September 2016 / Published online: 18 October 2016

Abstract We consider a turbulent channel flow, where a scalar point source with a time-harmonic intensity releases a substance that can be modeled as a passive scalar. With the source location known, our objective is to estimate the time history of the source intensity based on sensor measurements at different locations downstream of the source by adopting an adjoint approach. It is shown that the proposed algorithm reproduces the original coherent sinusoidal wave of the scalar source accurately from the chaotic scalar signals measured by our sensors. By systematically changing the source-sensor distance and the pulsation frequency of the source, we clarify how these two factors affect the estimation accuracy. The proposed scheme is also applicable to estimation with multiple sensors. We demonstrate that increasing the number of sensors improves the estimation greatly when the scalar

✉ D. Cerizza
davceriz@iis.u-tokyo.ac.jp

W. Sekiguchi
sekiguchi@daedalus.k.u-tokyo.ac.jp

T. Tsukahara
tsuka@rs.tus.ac.jp

T. A. Zaki
t.zaki@jhu.edu

Y. Hasegawa
ysk@iis.u-tokyo.ac.jp

[1] Institute of Industrial Science, The University of Tokyo, Tokyo, Japan

[2] Graduate School of Frontier Sciences, The University of Tokyo, Tokyo, Japan

[3] Department of Mechanical Engineering, Tokyo University of Science, Tokyo, Japan

[4] Department of Mechanical Engineering, Johns Hopkins University, Baltimore, MD, USA

is released from a source away from the wall, where large-scale eddies dominate the scalar dispersion. In contrast, the estimation performance remains poor even with multiple sensors when the scalar source is located near the wall, where the source information is quickly lost due to the strong turbulence activity and the scalar diffusion in the near-wall region.

Keywords Source characterization · Passive scalar transport · Channel flow · Inverse problem · Sensors · Direct numerical simulation

1 Introduction

Olfactory search strategies have a broad range of applications. Recently, they have attracted attention for identifying the location and intensity of the source of harmful chemical substances or pollutants released into the environment [1, 2]. In low-Reynolds-number flows, where molecular diffusion is dominant, spatial continuity of the chemical distribution and low advection velocities allow for search strategies based on the local concentration gradient to be successful. For high-Reynolds-number flows, a released agent is quickly dispersed into the turbulent medium, and the tasks of locating and characterizing the source become much more challenging [3].

Search strategies have been proposed in order to identify the location and intensity of a source using signals obtained by a series of sensors placed within the fluid domain [4, 5]. These methods can be classified into two categories: adaptive and model-based algorithms. Adaptive search algorithms are based on learning the relationship between the source characteristics and the sensor signals treating the fluid system as a black box [6, 7]. Most of them are inspired by the trajectories of animals and insects when searching for food or mating [8–10]. On the other hand, model-based approaches (e.g., Bayesian inference methods, minimum information entropy criteria, optimal sensor positioning, etc. [11–17]) extend the prediction capability of classical adaptive algorithms by explicitly incorporating the scalar transport equation. While such model-based algorithms are found to perform very well in simple and controlled environments, it is still uncertain how they perform in realistic scenarios (e.g. three-dimensional flows and complex geometries with obstacles) and in the presence of measurements errors [18]. Moreover, their superiority with respect to the intuitive nature-inspired adaptive approaches remains to be verified [19]. Meanwhile, recent rapid progress of numerical simulation techniques for turbulent flows and associated scalar transport enable detailed reproduction of the spatio-temporal evolution of complex flow and scalar fields. Utilizing such datasets, it is possible to achieve significant advancement in the efficacy of model-based scalar source identification algorithms.

The present work develops a model-based source characterization strategy, where the reconstruction of the time-trace of the source intensity is formulated as a variational problem. The algorithm requires the solution of an adjoint field in order to minimize a cost function representing the error between measured and estimated signals. We assume that the source location is known and the signal from a series of sensors placed in the flow field is used to iteratively correct the source intensity based on the adjoint field of the original physical (forward) problem.

The developed algorithm is tested in one of the most simplest canonical flows, namely, a fully developed turbulent channel flow. This flow configuration is chosen because huge information on turbulent statistics and flow structures has been accumulated during the last few decades. While the flow field is close to homogeneous turbulence around the center of the channel, it becomes more anisotropic due to strong shear with approaching the wall.

This allows us to evaluate the estimation performance in a systematic way by changing the distance of sensor and scalar source from the wall.

We consider an ideal situation in which the complete information of the entire velocity field in the search domain is known. First, we perform a forward simulation of turbulent scalar transport from a prescribed scalar source. Then, we record the time evolution of the concentration at the sensor location downstream, as well as the complete velocity field at each time step. In the second step, we attempt to reconstruct the scalar source intensity based on the sensor signal and the velocity information.

Throughout this work, uncertainties in the velocity field are not taken into account. Even in such an ideal situation, scalar source estimation is a difficult task, since the information on the scalar source is dispersed and diffused in space due to turbulent transport and molecular diffusion. The objective of the present study is to clarify how the rapid variation in time of the scalar source intensity and the source-sensors distance affect the estimation performance. In addition, we also discuss how the proximity of the source to the wall can affect the accuracy of the estimation.

2 Problem Setup

In the present study, a fully developed turbulent channel flow is considered. All variables are non-dimensionalized by the friction velocity u_τ and the half height of the channel h, while superscript $(.)^+$ is used to indicate quantities expressed in wall units. The computational domain is shown in Fig. 1. The streamwise, wall-normal and spanwise directions are denoted x, y and z, respectively. The dimensions of the computational domain are 5π and π in the x and z directions. A scalar source is present inside the channel and a series of k sensors are placed in the region downstream of the source in order to estimate its intensity. We consider the origin of our coordinate system to be on the bottom wall, as shown in Fig. 1. The source and the kth sensor positions are $\boldsymbol{x}_s$ and $\boldsymbol{x}_{m,k}$. The location of the kth sensor relative to the source is given by $\boldsymbol{x}_{m,k} - \boldsymbol{x}_s$.

We consider a Newtonian and incompressible fluid. The flow field is governed by the Navier-Stokes and continuity equations,

$$\frac{\partial u_i}{\partial t} + u_j \frac{\partial u_i}{\partial x_j} = -\frac{\partial p}{\partial x_i} + \frac{1}{Re_\tau} \frac{\partial^2 u_i}{\partial x_j \partial x_j}, \qquad \frac{\partial u_j}{\partial x_j} = 0. \tag{1}$$

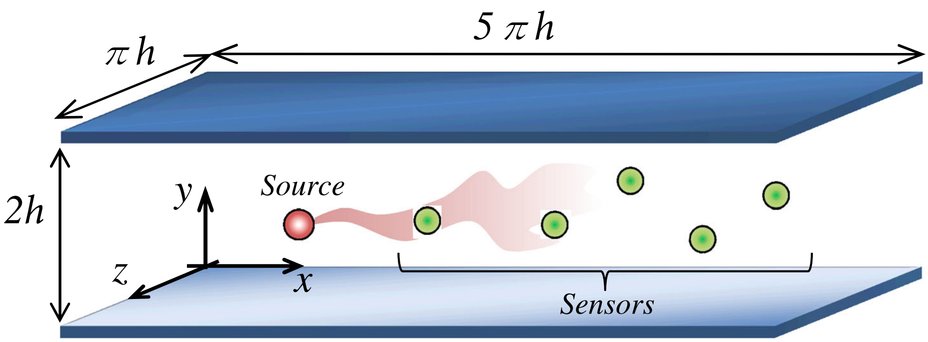

Fig. 1 Schematic of the computational domain and the coordinate system

The flow is driven by a constant pressure gradient. Although the Reynolds number of practical turbulent flows is typically high, we consider a moderate-Reynolds-number flow in order to validate and assess the present source reconstruction strategy. The friction Reynolds number is $Re_\tau \equiv u_\tau h/\nu = 150$, where ν is the kinematic viscosity. For the velocity field, periodic boundary conditions are applied in the streamwise and spanwise directions, while no-slip conditions are imposed at the top and bottom walls.

Figure 2 shows the time-averaged streamwise velocity profile $\overline{u}$ and the root-mean-square (RMS) value of the three velocity components compared with reference data from [20] at the same Re_τ. The good agreement between the present results and the reference data validates the present simulation.

Assuming a passive scalar, the scalar field $c(\mathbf{x}, t)$ is governed by the following advection-diffusion equation,

$$\frac{\partial c}{\partial t} + u_j \frac{\partial c}{\partial x_j} = \frac{1}{Pe}\frac{\partial^2 c}{\partial x_j \partial x_j} + \phi(t)\delta(\boldsymbol{x} - \boldsymbol{x}_s), \tag{2}$$

where Pe is the Péclet number, $\delta(.)$ is the Dirac's delta function, and $\phi(t)\delta(\boldsymbol{x} - \boldsymbol{x}_s)$ represents a scalar source located at $\boldsymbol{x}_s$ with an intensity that changes in time according to $\phi(t)$. In the most general case, the spatial function $\delta(.)$ centered at x_p is an arbitrary function with compact support which satisfies,

$$\int_\Omega g(\boldsymbol{x})\delta(\boldsymbol{x} - \boldsymbol{x}_p)d\Omega = g(\boldsymbol{x}_p) \qquad \textit{and} \qquad \int_\Omega \delta(\boldsymbol{x} - \boldsymbol{x}_p)d\Omega = 1,$$

where $g(\boldsymbol{x})$ is a generic function of space and Ω indicates the entire computational volume. In the present work we used a steep Gaussian function that satisfies the two conditions above and with a support extending over a few grid points in order to avoid the Gibbs effect that would arise by using a spatial delta function.

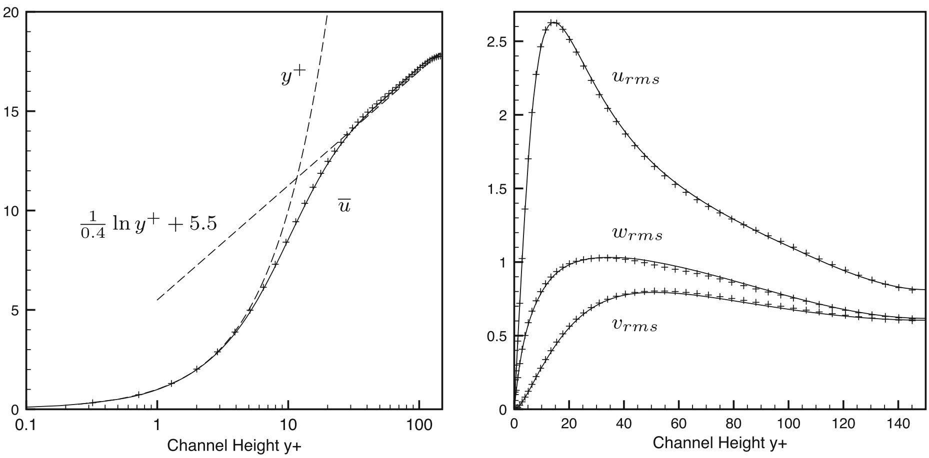

Fig. 2 Fundamental turbulent statistic in the present flow condition. At *left*: Mean velocity profile (*continuous line*) plotted together with the y^+ curve and Nijuradse's logarithmic law (*dashed line*). At *right*: root-mean-square values of fluctuating velocity components. *Symbols* and *continuous lines* represent respectively the present results and those from database [20] at the same Re_τ

The following boundary conditions are imposed on the scalar field,

$$c(\boldsymbol{x}, t = 0) = 0; \qquad \nabla c \cdot \boldsymbol{n} \left(\equiv \frac{\partial c}{\partial x_j} \cdot n_j \right) = 0 \; at \; \partial\Omega, \tag{3}$$

where $\partial\Omega$ and $\boldsymbol{n}$ represent the channel walls and their outward normal vectors, respectively. The no-scalar-flux boundary condition at the wall in Eq. 3 at right has been imposed in order to minimize the effect of the wall boundaries on the scalar field. In addition, In the streamwise and spanwise directions the scalar is removed in proximity of the domain boundaries in order to avoid it from re-entering at the opposite side by virtue of the periodic conditions in these two directions.

We consider the following time trace of the source,

$$\phi(t) = \frac{1}{2} \{1 + \cos(2\pi f t + \pi)\}. \tag{4}$$

The scalar source intensity is normalized by its maximum value. It should be noted that since the scalar transport equation (2) is linear, the amplitude of the scalar source does not affect the present results. Despite the fact that the present approach does not pose any constrain on the time trace of the source profile to be reconstructed, we use a single sinusoidal wave for $\phi(t)$. This choice provides the opportunity to assess how the accuracy of the scalar source estimation is affected by the frequency of the source and the streamwise separation of the sensor. We also note that any waveform of $\phi(t)$ can be expressed as a linear superposition of sinusoidal waves.

The Péclet number is chosen to be $Pe = Re_\tau$, which means the Schmidt Number is set to be unity, i.e., $Sc = Pe/Re_\tau = 1$. The flow and scalar fields are solved using a pseudo-spectral code for DNS of channel flow. For the spatial discretization, Fourier modes are employed in the streamwise and spanwise directions, while Chebyshev polynomials are used in the wall-normal direction. The number of modes employed in the streamwise, wall-normal and spanwise directions are $128 \times 65 \times 64$ respectively, which yields grid spacings $\Delta_x^+ \approx 12$, $0.08 < \Delta_y^+ < 4.9$, $\Delta_z^+ \approx 5$. The present numerical scheme and the grid resolution have been previously validated for DNS of turbulent scalar transport [21].

In general, both the source intensity and location are unknown. Here, however, we assume that the source location is given, so that only the time trace of its intensity $\phi(t)$ is sought. Using the signal collected on a single sensor located at $\boldsymbol{x}_m$ (or multiple sensors with positions $\mathbf{x}_{m,k}$) we aim to identify the function $\phi(t)$ which provides a signal that matches the measured one at the sensor location.

3 Characteristics of the Scalar Plume in the Forward Scalar Transport Problem

Figure 3 shows a series of contours for the scalar field plotted in the $x - y$ plane. In these figures, the release intensity is constant in time, and the source is placed at $y^+ = 150$ (A), $y^+ = 50$ (B) and $y^+ = 10$ (C) from the bottom wall. For each source location, the top panel shows an instantaneous view of the scalar field c, the middle panel shows the time-average of the scalar field $\overline{c}$ and the third panel shows contours of the RMS value of the scalar fluctuation c_{rms}.

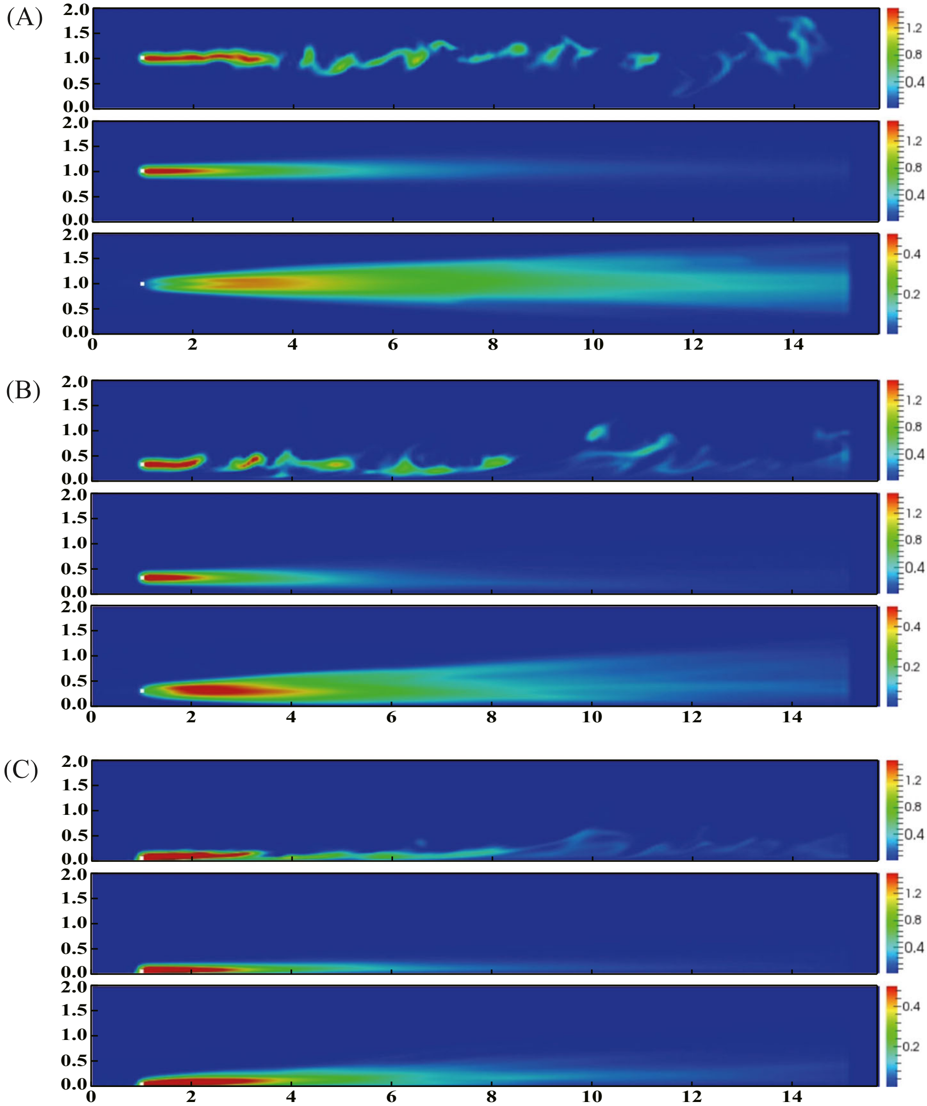

Fig. 3 Visualization of the scalar field released from a source with constant intensity placed at different distances from the bottom wall: $y_s^+ = 150$ (A), $y_s^+ = 50$ (B), $y_s^+ = 10$ (C). For each case three images are shown, from the *top* to the *bottom*: contour of the instantaneous scalar field c, of the time-averaged scalar field $\overline{c}$ and of scalar fluctuation c_{rms}. Contours are taken on the x - y plane. *White dots* are used to mark the source location

Due to turbulent transport, the scalar released is rapidly dispersed though the entire flow field. The plume, initially continuous in proximity of the source, separates into smaller patches which are transported along different paths downstream. Bigger patches break up into smaller ones due to the turbulent mixing, and the intensity of smaller patches decreases by the effect of molecular diffusion, up to the point where only a thin scalar trace remains.

The original signal leaving the source location therefore diminishes as it is advected within the flow.

Turbulent scalar transport phenomena can be characterized by two distinct processes, namely, dispersion and diffusion. The first effect causes the signal, which is initially concentrated at a single point, to be dispersed inside the channel wider volume. The second effect works locally, and damps the scalar field fluctuations at microscopic scales. It is important to clarify that the first phenomenon is simply the spatial dispersion of the source signal: if we are able to collect all the generated patches, we do not incur any deterioration of the original source signal. The second phenomenon, on the other hand, being the result of mixing at molecular level implies an attenuation of the source signal. In this case, we face an irreversible deterioration process, and we are not able to reconstruct the original source intensity time-trace, but only time-averaged properties of the source. This difference between dispersion and diffusion is captured in the scalar transport equation (2). The former is attributed to the advection term, while the latter to the molecular diffusion term. In the limit of an infinitely large Schmidt number, the latter effect can be neglected, so that the scalar is dispersed only due to the advection term. In such an ideal case, although the scalar patches would spread within the flow domain, the scalar concentration of each fluid element is maintained in time, so that the source information can in principle be reconstructed. It should be emphasized, however, that the two phenomena are generally coupled in reality. Therefore, it is possible that locally increased turbulence mixing causes break-up into small-scale scalar patches and the stretching of these patches, and consequently enhances the effectiveness of molecular diffusion.

While the instantaneous contours of c in Fig. 3 capture the first phenomenon, the effect of diffusion can be seen by considering the contours of the RMS value of scalar fluctuation c_{rms}. As the distance from the source increases the average intensity of the scalar decreases, together with the level of fluctuations measured by c_{rms}. In the case of a source with time-dependent intensity, we can expect to loose details of the source intensity profile, in particular high-frequency fluctuations, and to be able to reconstruct accurately the intensity profile of a rapidly changing source only in the region where c_{rms} is appreciable.

Different locations in turbulent channel flow are dominated by different transport mechanisms. This is evident in Fig. 3 showing how the instantaneous plume shape, the average c field and c_{rms} contours change when the source location moves closer to the wall (from A to C). While in the center of the channel transport is dominated by the motion of larger eddies and the dispersion of the plume, close to the wall the increased mixing leads to the occurrence of a region where diffusion effects become stronger. As a result, the extension of the plume of c_{rms} is smaller (C). Scalar fluctuations are indeed attenuated faster than the case with the source at the center of the channel (A).

While the effect of scalar dispersion on the source reconstruction process can be mitigated by collecting more information in the domain (i.e. adding more sensors), the deterioration of the source signal due to diffusion is more difficult to overcome, and the source-sensor distance must be reduced in order to increase the sensor sensitivity to the source.

4 Adjoint Approach for Estimation of the Scalar-Source Intensity

Identification of the source intensity history $\phi(t)$ can be formulated as a minimization problem of the following cost functional J, representing the difference between the predicted scalar concentration $c(\boldsymbol{x}_{m,k}, t)$ at the k^{th} sensor location $\boldsymbol{x}_{m,k}$ and the measurement $M(t)$, over the time horizon $t \in (0, T)$,

$$J \equiv \int_0^T \frac{1}{2} \sum_k \left\{ c(\boldsymbol{x}_{m,k}, t) - M(t) \right\}^2 dt. \tag{5}$$

An additional regularization term, penalizing the high-frequency temporal fluctuations of the source, is often implemented in the cost function above for similar inverse problems. The definition of the form and the weighting coefficient of this term, however, is not trivial, and selecting a not suitable value can translate in applying a low-pass frequency filter to the source, with the risk of canceling frequency contents of the source profile that we want to reconstruct. Since there is no systematic way of determining this term, and considering that our main purpose is to clarify how the source pulsation frequency affects the estimation performance, we decided to not include any regularization term, so that the estimated source intensity is purely determined by the sensing signal.

Minimizing J under the constraint of Eq. 2 is equivalent to minimizing the Hamiltonian,

$$H = J - \int_0^T \int_\Omega c^* \left\{ \frac{\partial c}{\partial t} + u_j \frac{\partial c}{\partial x_j} - \frac{1}{Pe} \frac{\partial^2 c}{\partial x_j \partial x_j} - \phi(t)\delta(\boldsymbol{x} - \boldsymbol{x}_s) \right\} dt d\Omega. \tag{6}$$

Here, $c^*(\boldsymbol{x}, t)$ corresponds to a Lagrange multiplier and is called the *adjoint* field. In order to consider variations due to a small change in the source intensity $\phi(t)$, we introduce the Fréchet differential,

$$H' = \frac{\mathscr{D}H}{\mathscr{D}\phi}\phi', \quad J' = \frac{\mathscr{D}J}{\mathscr{D}\phi}\phi', \quad c' = \frac{\mathscr{D}c}{\mathscr{D}\phi}\phi', \tag{7}$$

where the prime indicates a perturbation caused by an infinitesimal change in ϕ. Applying Fréchet differential to Eq. 6, we obtain

$$H' = J' - \int_0^T \int_\Omega c^* \left\{ \frac{\partial c'}{\partial t} + u_j \frac{\partial c'}{\partial x_j} - \frac{1}{Pe} \frac{\partial^2 c'}{\partial x_j \partial x_j} - \phi'(t)\delta(\boldsymbol{x} - \boldsymbol{x}_s) \right\} dt d\Omega. \tag{8}$$

Applying integration by parts to Eq. 8, we reach the following expression:

$$H' = c' \left\langle \left\{ \frac{\partial c^*}{\partial t} + \frac{\partial c^* u_j}{\partial x_j} + \frac{1}{Pe} \frac{\partial^2 c^*}{\partial x_j \partial x_j} + \sum_k Er_k(\boldsymbol{x}, t)\delta(\boldsymbol{x} - \boldsymbol{x}_{m,k}) \right\} + \phi' c^* \delta(\boldsymbol{x} - \boldsymbol{x}_s) \right\rangle + \mathscr{B}, \tag{9}$$

where $Er_k(x, t) = c(\boldsymbol{x}_{m,k}, t) - M(t)$ is the error of the predicted scalar at the sensor, $c(\boldsymbol{x}_{m,k}, t)$, with respect to the true measurement, $M(t)$. The error is expressed as a function of both $\boldsymbol{x}$ and t to be included in the spatio-temporal integral. The brackets $< . >$ indicate the spatio-temporal integration over Ω and $t \in (0, T)$. The last term in Eq. 9, namely $\mathscr{B}$, is a boundary term,

$$\mathscr{B} = \left\langle -\frac{\partial \left(c^* c'\right)}{\partial t} - \frac{\partial \left(c^* c' u_j\right)}{\partial x_j} + \frac{1}{Pe} \frac{\partial}{\partial x_j} \left(c^* \frac{\partial c'}{\partial x_j} - c' \frac{\partial c^*}{\partial x_j} \right) \right\rangle. \tag{10}$$

It should be noted that $\mathscr{B}$ has a divergence form, so its time-volume integration is equivalent to the boundary integral. As with the scalar field c, the adjoint scalar is also removed in the streamwise and spanwise directions in proximity of the domain boundaries and therefore both c and c^* are equal to zero at these locations. Considering the boundary conditions for Eq. 3 and the fact that $\boldsymbol{u}$ is zero at the walls, in order for $\mathscr{B}$ to vanish it is required to apply the following initial and wall boundary conditions:

$$c^*(\boldsymbol{x}, t = T) = 0, \qquad \nabla c^* \cdot \boldsymbol{n} = 0 \; at \; \partial\Omega. \tag{11}$$

By setting the first term in Eq. 9 to zero, the following adjoint equation for the scalar field is obtained,

$$\frac{\partial c^*}{\partial t} + \frac{\partial (c^* u_j)}{\partial x_j} = -\frac{1}{Pe}\frac{\partial^2 c^*}{\partial x_j \partial x_j} - \sum_k Er_k(\boldsymbol{x}, t)\delta(\boldsymbol{x} - \boldsymbol{x_{m,k}}). \tag{12}$$

By introducing the new time coordinate, $t^* = T - t$, the above equation can be recast as a forward problem in t^*, with positive diffusion. In terms of the new time variable, the adjoint equation becomes,

$$\frac{\partial c^*}{\partial t^*} - \frac{\partial (c^* u_j)}{\partial x_j} = \frac{1}{Pe}\frac{\partial^2 c^*}{\partial x_j \partial x_j} + \sum_k Er_k(\boldsymbol{x}, t)\delta(\boldsymbol{x} - \boldsymbol{x_{m,k}}) \tag{13}$$

which represents the advection-diffusion equation for the adjoint field c^*, with similar computational complexity as the forward problem for c, and using the same velocity data with opposite sign. When the adjoint equation (13) is solved subject to the above initial and boundary conditions, Eq. 9 becomes

$$H' = \left\langle \phi' c^* \delta(\boldsymbol{x}) \right\rangle. \tag{14}$$

In order to ensure that H' decreases, the scalar source is updated according to the following formula,

$$\phi'(t) \left(\equiv \phi^{n+1}(t) - \phi^n(t) \right) = -\alpha c^*(0, t), \tag{15}$$

where α is a positive coefficient. A straightforward approach to determine the optimal value of the coefficient α is presented in Appendix A.

As a first step, a series of forward simulations of scalar transport from point sources with different pulsating frequencies are carried out. The resultant reference signal at each sensor location is obtained. These data represent the measurement profiles $M(t)$ to be matched. The full spatio-temporal data of the velocity field in the computational domain throughout an entire time horizon is also stored during this initial run and used in all subsequent ones (for both forward and adjoint scalar field calculations). No measurement errors are included in this study.

Given an arbitrary initial source profile $\phi(t)^0$, the herein presented algorithm requires between 4 and 8 iterations (one iteration entails a forward-adjoint loop) to accurately reconstruct the source profile. The total simulated time horizon is equal to 3 time units, and it has been chosen in order to include at least 6 full periods of the source profile at the lowest frequency considered ($f = 2$).

5 Results and Observations

5.1 Single sensor

We first consider the results for a single sensor. A single source is located at the center of the channel, i.e., $(x_s, y_s, z_s) = (1, 1, \pi/2)$, which corresponds to a distance from the walls equal to $y_s^+ = 150$. The sensor is placed directly downstream of the source. The source intensity pulses with the sinusoidal profile given by Eq. 4. Both the source pulsating frequency f and the source-sensor distance $x_m - x_s$ are systematically changed, $f = 2, 4, 8, 16$ and $x_m - x_s = 3, 6, 9, 12$, in order to assess the effect of these two parameters on the performance of our algorithm.

Figure 4(A) shows the scalar field in the x - y plane at the center of the channel in the forward (physical) simulation with the source pulsating frequency of $f = 4$. The contour is a visualization of the instantaneous scalar field taken at time $t = 2$ and clearly shows how the scalar is dispersed and diffused by the turbulent flow field. Below in the same figure, contours of the instantaneous adjoint fields generated by each sensor at $x_m - x_s = 3$, 6, 9 and 12 from the source are shown in Fig. 4 (B - E) respectively. Time is equal to $t^* = T - 2$, and all figures correspond to the first iteration of our algorithm. The adjoint field appears as a series of negative scalar patches released from the sensors and advected upstream by the same velocity field of the reference case with an opposite sign (see, Eq. 13). As these patches cross the source location, they provide the time trace of the gradient of $\phi(t)$ that is used to update the source profile after each forward-adjoint loop (see, Eq. 15). With subsequent iterations, the error between measured and estimated signals at the sensor location progressively decreases, and therefore the intensity of the adjoint scalar field also reduces. When the error vanishes, the adjoint scalar field is also nullified (see, Eq. 13).

Figure 5 shows the time traces of the scalar source and sensor signals obtained for the same case with $f = 4$. At left the true source profile (dashed line) is compared with the reconstructed profile (continuous line), while at right the reference sensor signal (dashed line) is compared with the one obtained by performing a forward simulation using the reconstructed source (continuous line). From top to bottom, the source-sensor distance is increased $x_m - x_s = 3$, 6, 9 and 12. The intensity of the original scalar source is captured only for certain time instants, and the estimated scalar source contains a higher

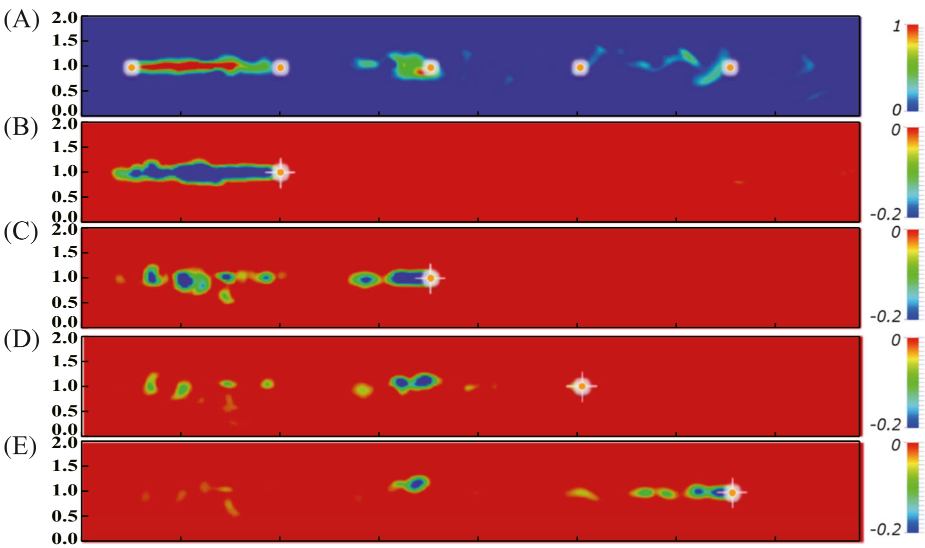

Fig. 4 Contour of scalar field c in the x - z plane at the center of the channel in the case of $f = 4$. (A): reference forward scalar field at t = 2. (B)-(E): adjoint scalar field c^* generated in the first iteration process at sensor locations of $x_m - x_s = 3$ (B), 6(C), 9(D), 12(E). Time is $t^* = T - 2$. Source and sensor positions are marked with yellow dots.

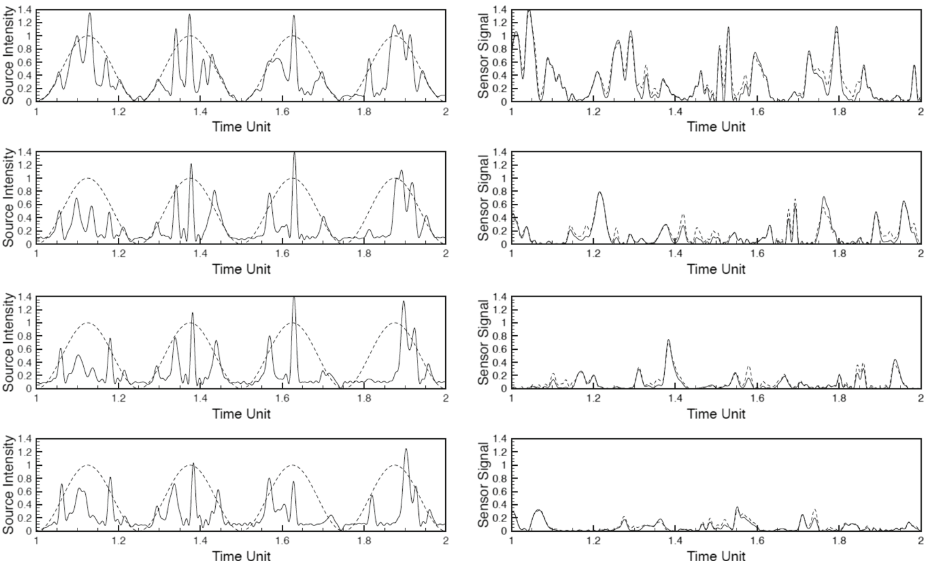

Fig. 5 Source profile and sensor signal for the case $f = 4$. From the top to the bottom, the distance sensor-source increases as $x_m - x_s = 3$, 6, 9 and 12. At *left*: comparison between the true sinusoidal source profile (*dashed line*) and the estimated source profile (*continuous line*); at *right*: comparison between the measurement (*continuous line*) and reconstructed (*dash line*) sensor signal. Only data within the time frame $t = 1$ - 2 are shown

frequency noise. Since measurement and modeling errors are not part of this calculation, the observed estimation error can be attributed to the dispersion and diffusion effects discussed in Section 3.

At the right side of Fig. 5, where the reference sensor signal is compared with the estimated one, we observe very good agreement between the two profiles. On one hand, this confirms that our algorithm is correctly modifying the source in order to match the reference data. On the other hand, this observation supports the more important conclusion that, with only one sensor available, different scalar source profiles can give a similar signal at the sensor location. In particular, it is clear that for specific time instants the reconstructed time trace of the source intensity is very low compared to the true profile despite the fact that the signal at the sensor location matches the reference sensor profile. This is because the scalar patches released at these particular instants do not pass by the sensor location, so that no significant sensor signal is obtained. In such cases, no clue regarding the source information can be obtained, and therefore the source intensity is not accurately reconstructed.

Figure 6 shows at left the frequency spectra of the reconstructed source traces, $E_\phi(f)$, and at right the spectra of the reference signals at the sensor, $E_s(f)$, for the different $x_m - x_s$ considered with fixed $f = 4$. The mean value has been subtracted from the data before the spectral analysis in order to remove the component at zero frequency. We can clearly see that the single frequency $f = 4$ carried by the original sinusoidal source profile is accompanied by a wider range of frequencies. However, it is particularly interesting to note that, while the intensity of this component steadily decreases in the sensor signal with increasing distance x_m, it remains prominent in all the reconstructed source profiles. This underlines how our algorithm is able to reconstruct the main frequency of the true source intensity profile despite the deterioration of the signal at the sensor location for increasing x_m.

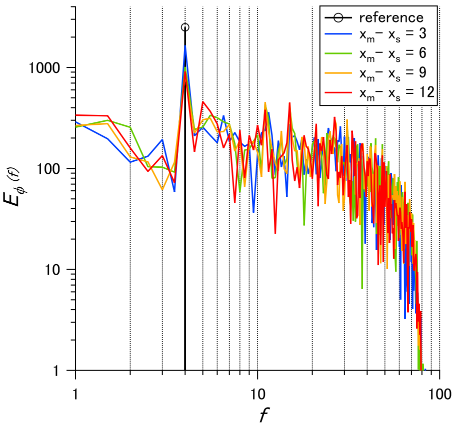

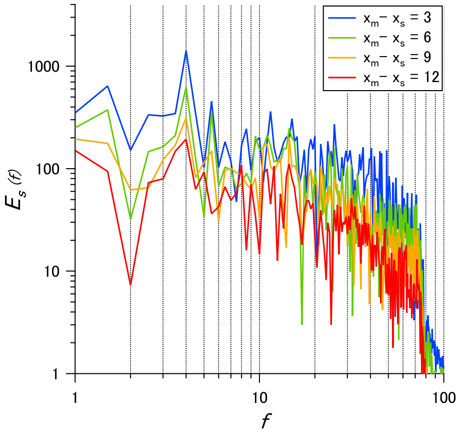

Fig. 6 Frequency spectra of the reconstructed source profiles (*left*) and of the reference sensors signals (*right*) generated by the true source. Source frequency $f = 4$. In the figure on the left, a circle has been used to represent the single frequency content of the true source

In order to quantitatively evaluate the estimation performance for each combination of source frequency and source-sensor distance, we introduce two performance indices, namely, the correlation coefficient and L2-norm between the true (ϕ_{true}) and reconstructed (ϕ_{rec}) source intensity profiles. These two quantities are defined as,

$$R_{\phi_{true}\phi_{rec}} \equiv \frac{\left(\int(\phi_{true}(t) - \bar{\phi}_{true})(\phi_{rec}(t) - \bar{\phi}_{rec})\right)^2}{\int(\phi_{true}(t) - \bar{\phi}_{true})^2 \int(\phi_{rec}(t) - \bar{\phi}_{rec})^2}$$

$$L_{2,\phi_{true}\phi_{rec}} \equiv \frac{1}{T}\int_0^T \|\phi_{true}(t) - \phi_{rec}(t)\|^2,$$

where the overline indicates time-average quantities.

In Fig. 7, the correlation coefficient (left) and L2-norm of the error (right) are presented as a function of $x - x_s$ and f. Along the horizontal axis the source frequency f changes from 2 to 16, while on the vertical axis the sensor distance x_m increases from 3 to 12. It is clear how the estimation capability decreases with increasing the frequency of the source and the source-sensor distance. Both parameters contribute to enhancing the dispersion of the scalar before it reaches the sensor. However, the contours shown in Fig. 7 underline that when $x - x_s$ is short, the decrease in estimation performance is mainly influenced by the source-sensor distance (contour lines are nearly horizontal for $x_m = 3$ - 6), while as x_m is further increased both parameters jointly influence the estimation performance.

In order to distinguish between the effects of the source-sensor distance and the pulsating frequency on the estimation performance, we plot in Fig. 8 the time-averaged concentration and scalar fluctuation along the line connecting the source and sensor. Note that these statistics are integrated for a sufficiently long period to ensure their convergence. While the average scalar concentration can be directly correlated to the probability to catch a signal at a given location, the RMS value of scalar fluctuations is a measure of the transient content of the scalar signal, and thus the portion of the signal that contains the time variable information about the source. The average scalar concentration is independent of the source frequency and decreases rapidly moving away from the source. This causes a rapid deterioration of the present estimation performance due to the lack of signal at the sensor.

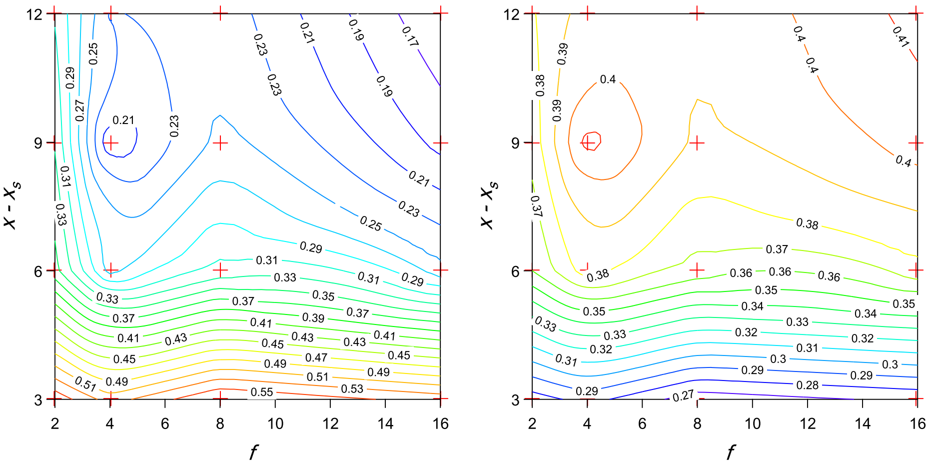

Fig. 7 Correlation coefficient (*left*) and L2-norm (*right*) of true and reconstructed source intensity profile. Source frequency changes along the horizontal axis as $f = 2, 4, 8$ and 16, while along the vertical axis the source-sensor distance increases as $x_m - x_s = 3, 6, 9$ and 12. Red marks indicate the performed cases

The effect of the source frequency, on the other hand, appears only in the scalar fluctuation shown in Fig. 8 at right, and becomes relatively larger with increasing the source-sensor distance. This can be attributed to the fact that the scalar patches released at a higher frequency have smaller spatial scales, and this enhances the scalar dissipation. The present result suggests that slight deterioration of the estimation performance with increasing the pulsation frequency observed in Fig. 7 can be linked to the lower scalar fluctuations, or larger scalar dissipation, in forward simulation.

Another interesting comparison between the true and reconstructed source profiles can be made by comparing their time-averaged values. While the correlation coefficient and L2-norm can provide a measure of the discrepancies between the shapes of the true and

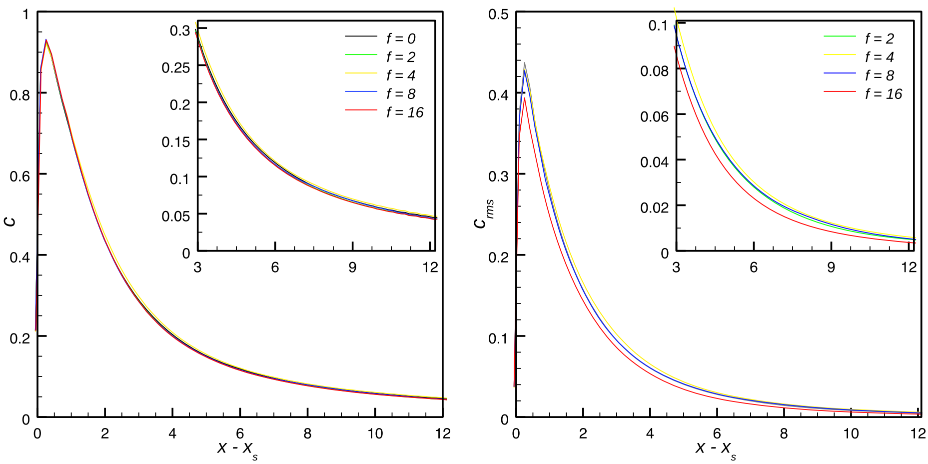

Fig. 8 Statistics of the scalar field plotted along a line connecting the source and sensor for different source frequencies f. *Left*: time-averaged scalar concentration. *Right*: RMS value of scalar fluctuation

reconstructed profiles, the average value is a measure of the amount of scalar released per unit time from the source. If we imagine the scalar to be a pollutant for example, it is clear how the ability to estimate this quantity is crucial in order to identify its impact on the surrounding environment. In the range of source pulsation frequencies considered, this average intensity is not sensitive to the source frequency, and decreases with increasing source-sensor distance. It varies from 0.38 for $x_m - x_s = 3$ down to 0.28 for $x_m - x_s = 12$. Since the average of the true profile is 0.5, the estimated amount of released scalar is 24 % to 44 % lower than its actual value. This large error can be attributed to the dispersion of the scalar patches by the turbulent transport once released from the source. The measurement by a single sensor is not sufficient to accurately estimate the amount of released scalar. This problem can be overcome by introducing multiple sensors as discussed below.

5.2 Multiple sensors

The algorithm presented in Section 4 can make use of the measurements from multiple sensors without additional computational cost relative to the case with one sensor. The adjoint equation to be solved in this case will simply include multiple forcing terms of the right hand side, one for each sensor. Here, we examine how the use of multiple sensors can be beneficial when reconstructing the source intensity profile using measurements far away from the source.

We consider a series of 17 sensors placed at a fixed downstream distance $x_m - x_s = 12$ and distributed in the cross-flow plane. We place multiple sensors within the scalar wake downstream of the source such that they collect most of the released scalar. A single sensor is then placed directly downstream of the source. Then, a first set of sensors is placed around the first one plus a second set in the outer region of the scalar plume. The pattern used for the 17 sensors is shown in Fig. 9, and the detailed information on the sensor locations can be found in Appendix B.

Figure 9 shows an instantaneous visualization of the forward and ajoint field. The source pulsating frequency is set to be $f = 4$. Iso-surfaces of the instantaneous scalar field c from the reference forward simulation and the adjoint field c^* for the first backward simulation are shown in blue and red, respectively. Each scalar patch crossing a sensor location in the forward simulation at time t defines a forcing term in the adjoint equation at the corresponding sensor location in the backward simulation at time $t^* = T - t$ (see Eq. 13).

Figure 10 compares the true and reconstructed source intensity profiles after 6 iterations. The reconstructed source intensity profile agrees the true one better than that estimated by a single sensor when $f = 4$, $x_m - x_s = 12$, shown in Fig. 5 in Section 5.1. The correlation coefficient of the reconstructed and true profiles is 0.832 while the L2-norm of the error is 0.152. Estimation of the amount of scalar released is 0.455 and the prediction error is 9 %, which is also improved with respect to the single sensor case.

By using multiple sensors the amount of information collected from the flow field increases. The use of multiple sensors increases the probability of intercepting scalar patches that would be missed by a single sensor.

5.3 Source placed at different channel heights

In this section we investigate the performance of the algorithm when the source is placed at different channel heights. While large-scale eddies dominates turbulent scalar dispersion around the center of the channel, moving closer to the wall, smaller-scale eddies become

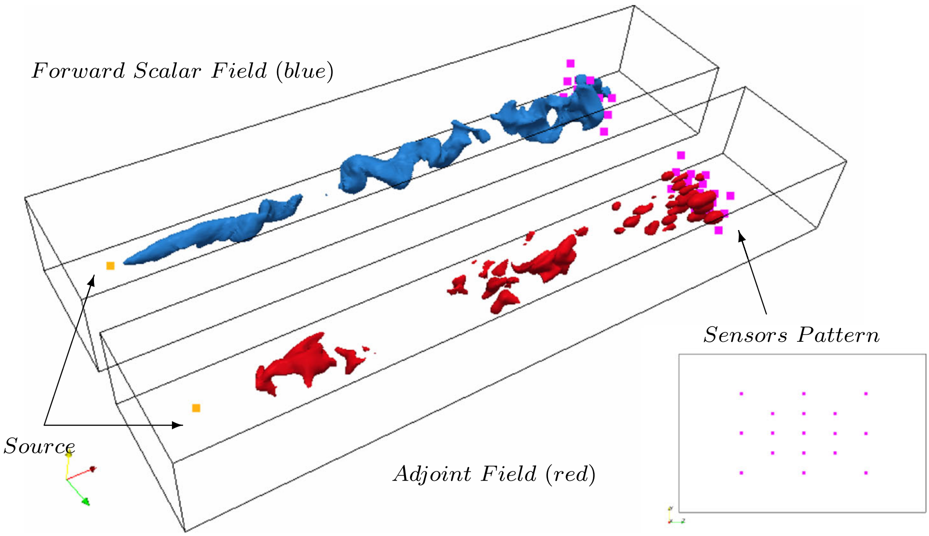

Fig. 9 Iso-surfaces of the forward scalar field (*blue*) produced by the true source profile, and adjoint field (*red*). Source location is $y_s^+ = 150$ from the bottom wall. In the figure at the bottom right: locations of the 17 sensors on the cross-flow plane at $x - x_s = 12$

more dominant and the presence of near-wall turbulence structures changes the transport mechanism. They influence the present estimation performance.

We first consider two heights: $y_s^+ = 50$ and $y_s^+ = 10$. The first location is closer to the wall but still outside the buffer layer, while the second is inside it. We again use 17 sensors at the downstream distance of 12 from the source, with a stencil similar to the one used in Section 5.2 maintaining one sensor directly downstream of the source with an inner and outer rings of sensors, but we deform the stencil slightly in order to fit it close to the wall. Images of the instantaneous scalar fields and source profiles comparisons are shown in Fig 11, 12 for the case with $y_s^+ = 50$ and Figs 13, 14 for the case with $y_s^+ = 10$. The pulsating frequency of the source is set to be $f = 4$.

In Figs. 11 and 13 the iso-surfaces of the reference forward scalar field c and of the backward adjoint field c^* are depicted in blue and red, respectively. In the first case, with the source placed at $y_s^+ = 50$ from the bottom wall, the different scalar patches, released at each pulsation of the source, are still separated and identifiable. In the second case, with

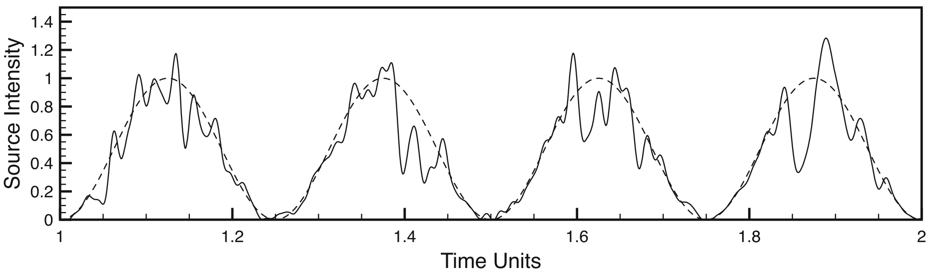

Fig. 10 Comparison between the true (*dashed line*) and reconstructed (*continuous line*) source profiles, $f = 4$, multiple sensors, source location is $y_s^+ = 150$

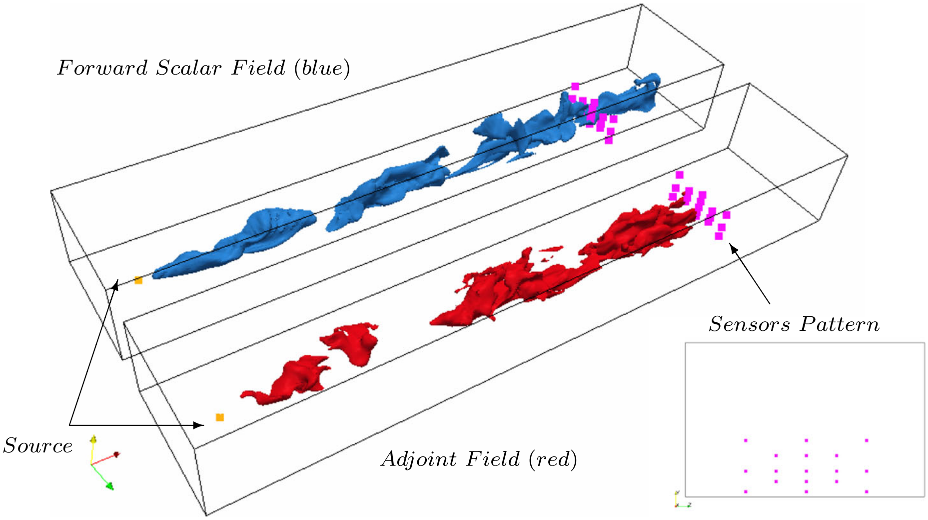

Fig. 11 Iso-surfaces of the forward scalar field (*blue*) produced by the true source profile, and adjoint field (*red*). Source location is $y_s^+ = 50$. In the figure at the bottom right: locations of the 17 sensors on the cross-flow plane at $x - x_s = 12$

the source in the buffer layer, the increased stretching and low velocities close to the wall enhance diffusion of the original signal, with the scalar patches becoming indistinguishable. This change in the transport mechanism that occurs close to the wall causes an irremediable loss of information about the source intensity history.

In Figs. 12 and 14 the true and reconstructed source intensities are compared. In Fig. 12, even though the source has been moved towards the wall, at $y_s^+ = 50$, the main scalar transport remains dominated by the larger eddies. As a result, the effect of the wall is still inappreciable, and does not adversely affect the performance of our algorithm. The correlation coefficient of the true and reconstructed source profiles is kept high as 0.808 and the L2-norm error is as low as 0.157, while the average intensity of the reconstructed source is 0.476, within 5 % from the true value (Fig. 13).

In Fig. 14 on the other hand, it is clear that relocating the source down inside the buffer layer changes the transport mechanism and deteriorates the original signal, loosing de facto

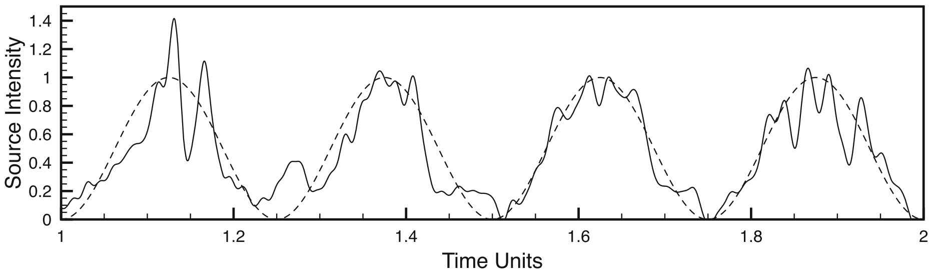

Fig. 12 Comparison between the true (*dashed line*) and reconstructed (*continuous line*) source profiles, $f = 4$, multiple sensors, source location is $y_s^+ = 50$

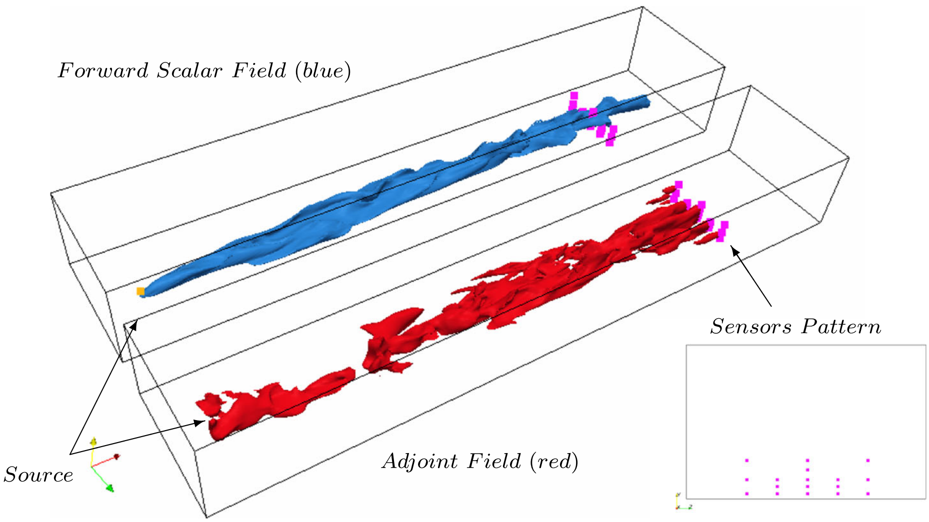

Fig. 13 Iso-surfaces of the forward scalar field (*blue*) produced by the true source profile, and adjoint field (*red*). Source location is $y_s^+ = 10$ from the bottom wall. In the figure at the bottom right: locations of the 17 sensors on the cross-flow plane at $x - x_s = 12$

any chance to reconstruct the time trace of the original source intensity. The poor estimation performance is quantified by the correlation coefficient, $R_{\phi\phi} = 0.151$ and the L2-norm, $L_2 = 0.326$. The time-average of the reconstructed source intensity is however 0.513, which is within an error of 3 % of the true value. This means that despite the fact that we are collecting sufficient scalar to be able to estimate correctly the average source intensity, the signal reaching our sensor has deteriorated to the point where an accurate reconstruction of the true time trace of the source becomes impossible.

In order to identify a possible scaling of the algorithm performance as a function of the distance from the wall, the performance of the algorithm is plotted along the channel height in Fig. 15. Additional calculations have been carried out placing the source at $y_s^+ = 20$ and $y_s^+ = 30$, always using 17 sensors. The resultant correlation coefficient is normalized

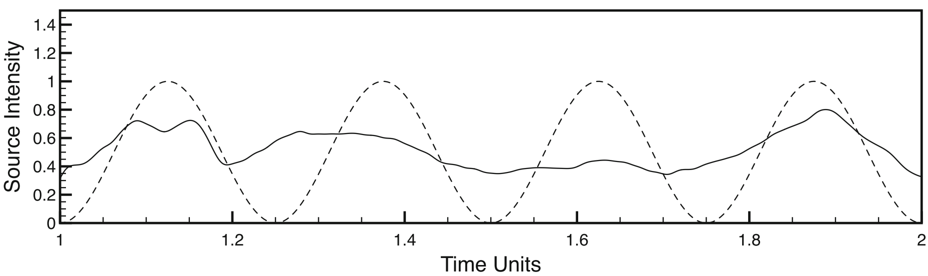

Fig. 14 Comparison between the true (*dashed line*) and reconstructed (*continuous line*) source profiles, $f = 4$, multiple sensors, source location is $y_s^+ = 10$

by the value obtained when the sensor and source are located at the center of the channel as $R_{\phi\phi}/R_{\phi\phi\ y^+=150}$. At left, the performance is compared with the weighted average of the RMS values of scalar fluctuation at all sensor locations. This is defined as:

$$C_{rms} = \frac{\sum_k c_{rms}(x_{m,k}) * \overline{c}(x_{m,k})}{\sum_k \overline{c}(x_{m,k})}. \tag{16}$$

As the source is moved close to the wall, C_{rms} decreases. This causes deterioration of the algorithm performance. In Fig. 15 at right, a comparison between the same performance curve and a measure of the mean shear $1 - d\overline{u}/dy^+$ is presented. Due to the normalization by the wall-unit, its value is 0 at the wall and 1 at the center of the channel. The decrease in performance as we approach the wall is qualitatively similar to the trend in $1 - d\overline{u}/dy^+$. The mean shear stretches the scalar patches that becomes more and more intense as the source approaches the wall. As a result, molecular diffusion is more effective close to the wall. This effect should be the main cause of decrease in performance close to the wall. In addition, the reduced advection velocity close to the wall increases the time required to cover the distance between the source and the sensors, allowing for a longer time for the molecular viscosity to degrade the scalar signal.

A similar effect of the mean shear on the velocity and scalar fields close to the wall is presented in [22] and [23], where it is shown that the mean shear enhances viscous/scalar dissipation so that high-frequency fluctuations are suppressed, whereas only low-frequency fluctuations can penetrate the near-wall layer.

5.4 Measurement errors

So far, we have investigated the estimation performance without measurement and modeling errors. Although detailed analyses of these uncertainties are left for future work, we briefly address here how the measurement noise affects the present estimation performance. This

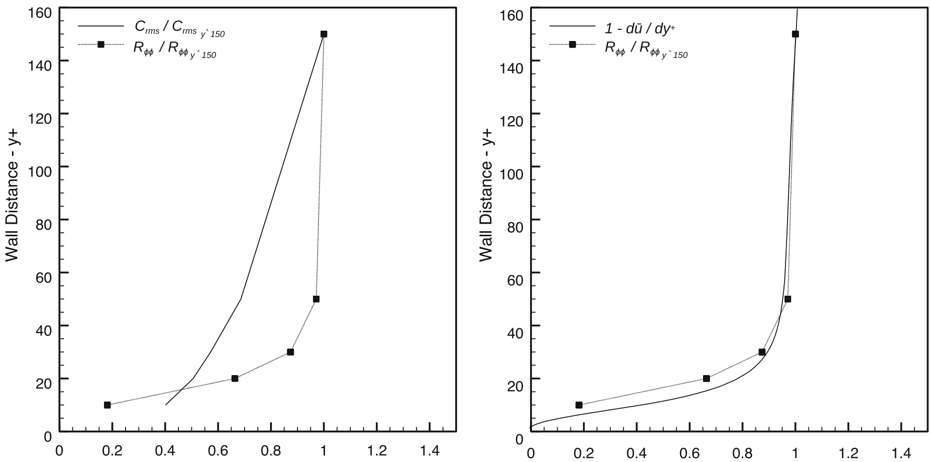

Fig. 15 Comparison between the estimation performance with turbulence properties. The correlation coefficient between the reconstructed and true source profiles are plotted by solid squares together with the RMS values of scalar fluctuation (*left*) and the mean shear (*right*). All variables are normalized by the values at the channel center

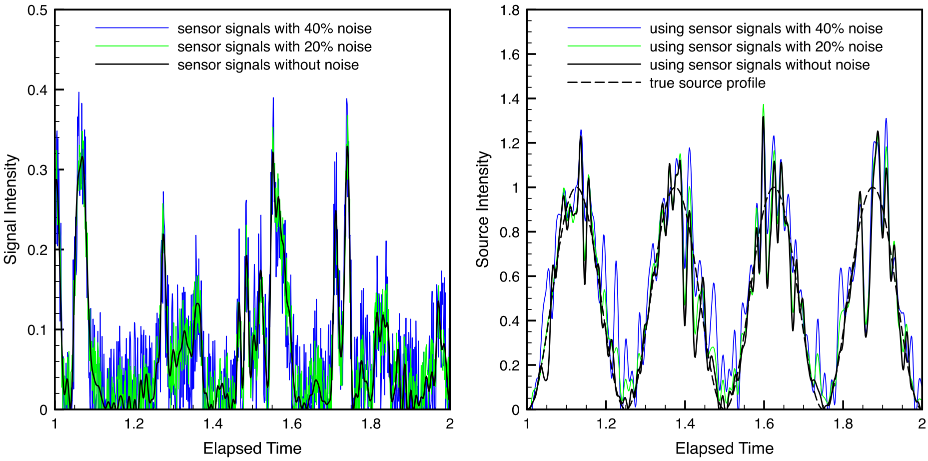

Fig. 16 Comparison between the unperturbed and perturbed signal for the sensor with maximum intensity (*left*) and comparison between the reconstructed source intensity profile when using unperturbed and perturbed measurements (*right*). Only a limited time frame of the entire time horizon considered is shown

was done by adding random noise with normal distribution to all 17 sensor signals. The RMS value of the noise is set to be 20 % and 40 % of the maximum of the averaged scalar signals among 17 sensors. For this analysis, a source with frequency $f = 4$ was located at the center of the channel ($y^+ = 150$), and the same arrangement of 17 sensors previously adopted for this configuration was used (see Appendix B).

The results are presented in Fig. 16. At left, the unperturbed and perturbed signals for the sensor with maximum time-averaged intensity are shown. A large separation in frequency can be confirmed between the added noise and the original signal. At right, the reconstructed source profile obtained using the unperturbed measurements is compared with the one obtained with perturbed signals. As can be seen, the effect of measurement errors on the reconstructed signal is not significant The correlation coefficient between the true source and its reconstruction using unperturbed measurements is 0.874, and it decreases to 0.873 (< 1 %) and 0.805 (-8 %) in presence of the noise with its magnitude of 20 and 40 %, respectively.

The proposed algorithm is therefore robust to high-frequency measurement errors (i.e. noise), since high-frequency fluctuations in the adjoint scalar forcing term are rapidly damped. It is interesting to contrast the effect of high frequency source terms in the adjoint (measurement) and the forward (source) equations. In the adjoint, the rapid damping eliminates measurement errors and enhances robustness of our algorithms. On the other hand, in the forward problem the scalar signal from a rapidly oscillating source decays quickly and is therefore difficult to reconstruct.

6 Conclusions

In the present work, we introduced an algorithm to reconstruct the time trace of the intensity of a scalar source at a known location inside a fully developed turbulent channel flow. The time trace of source intensity was given by a sinusoid with different frequencies, and was reconstructed using a series of sensors downstream.

While the reconstructed source profile can generate signals at the sensors locations that perfectly match the measurements, the difference in the true and reconstructed source profiles indicates that part of the information on the scalar source is lost during turbulent transport processes. The reconstruction performance is generally affected by two phenomena: scalar dispersion and diffusion. The former represents convective transport which separates an initially continuous plume into small scalar patches. The latter represents an irreversible process caused by molecular diffusion that eliminates spatial inhomogeneities in the scalar field.

In the single sensor case, the source reconstruction performance deteriorates when increasing the source-sensor distance and the source pulsation frequency. While both these parameters jointly cause a decrease in performance, the source-sensor distance dominates when $x_m - x_s < 6$, whereas the effect of the pulsation frequency emerges only at larger distances. The rapid decrease in performance due to scalar dispersion can be correlated to the rapid reduction in the average scalar concentration, while the effect of the source frequency far from the source is due to the suppression of scalar fluctuations, which is enhanced with increasing the pulsating frequency. The discrepancy between the time-averaged intensities of the true and reconstructed source suggests that a single sensor cannot accurately estimate the amount of scalar released. This is due to a large amount of scalar not crossing the sensor location.

In order to mitigate the effects of dispersion, we examined how increasing the number of sensors can reduce the loss of information. This does not require any additional computational cost for the proposed algorithm, since the use of multiple sensors translates only into having multiple forcing terms in the adjoint field calculation. With multiple sensors the source profile can be accurately reconstructed even with sensors located at large distances from the source ($x - x_s = 12$).

While the center of the channel is dominated by the turbulent transport realized by the larger eddies, close to the wall the transport mechanism changes, and diffusion effects become stronger since the advection velocity is low and the scalar patches are stretched more significantly by the mean shear. In order to investigate the performance decrease in this flow regime, additional simulations were performed placing the source inside the buffer layer, at $y^+ = 10$. In this configuration, when the sensors are far from the source ($x - x_s = 12$), it is not possible to reconstruct the source profile with sufficient accuracy. The reconstruction of its average intensity, however, is still accurate.

The robustness of the algorithm to a random noise on the measurement has been verified. In presence of high-intensity noise the correlation coefficient between the reconstructed and true source profiles reduces with respect to the case that used unperturbed measurements by less than 10 % only. A diffusive property of the adjoint equation helps in this case, damping high-frequency fluctuations generated by noisy forcing terms.

We verified the effectiveness of the proposed algorithm, and evaluated how dispersion and diffusion affects the accuracy of the source reconstruction. Loss of information due to dispersion is mitigated by using additional sensors. Diffusion, on the other hand, leads to an irreversible loss of information, and precludes the possibility of reconstructing accurately the time-trace of the source.

The present study considers ideal situations, where the full velocity information is available. It is of great interest how the estimation performance is affected by uncertainties in the velocity data. In addition, we assumed that the source location is given, whereas in many applications it is unknown. The present estimation strategy can be extended to these problems. Moreover, the multiple sensors have been arranged in the present work in an ad-hoc manner, and therefore an optimal arrangement should be sought in future work.

Acknowledgments This study is supported by the Japan Science and Technology Council (JST), Strategic International CollaborativeResearch Program (SICORP), and by the National Science Foundation (grant CNS 1461870)

Appendix A: Optimal Value of the Coefficient α

As shown in Eq. 15, $c^*(0,t)$ provides only the *direction* to modify the current estimate of ϕ, whereas the optimal amplitude α is unknown. However, we can exploit the linearity of the scalar transport equation (2) to derive the optimal value of α with the following procedure:

- Assuming $c^n(\boldsymbol{x}_{m,k},t)$ is the current estimate of the scalar field at the k^{th} sensor location (superscript n identifies the current iteration number), the error $Er_k(t)$ at the sensor is given by the difference between the prediction and the measurement, i.e., $Er_k^n(t) = c^n(\boldsymbol{x}_{m,k},t) - M(t)$.
- We solve the adjoint equation (13) with $Er_k^n(t)$ as a source term at each sensor location, and the resulting adjoint field at the source location, $c^*(0,t)$, is obtained.
- Instead of updating the source intensity in accordance with Eq. 15 using an ad-hoc value of α, we first solve a forward equation (2) with scalar source term $\phi(t) = c^*(0,t)$ (i.e. $\alpha = 1$), and store the response $\tilde{c}(\boldsymbol{x}_{m,k},t)$ at the sensor location $\boldsymbol{x}_s$.
- With $\tilde{c}(\boldsymbol{x}_s,t)$, the predicted concentration $c^{n+1}(\boldsymbol{x}_{m,k},t)$ at the sensor location for an arbitrary value of α can be expressed as,

$$c^{n+1}(\boldsymbol{x}_{m,k},t) = c^n(\boldsymbol{x}_{m,k},t) - \alpha\tilde{c}(\boldsymbol{x}_{m,k},t).$$

- Hence, the cost function J in the next time step $(n+1)$ is given by,

$$\begin{aligned}
J^{n+1}(t) &= \int_0^T \frac{1}{2}\sum_k \left\{c^{n+1}(\boldsymbol{x}_{m,k},t) - M(t)\right\}^2 dt \\
&= \int_0^T \frac{1}{2}\sum_k \left\{c^n(\boldsymbol{x}_{m,k},t) - \alpha\tilde{c}(\boldsymbol{x}_{m,k},t) - M(t)\right\}^2 dt \\
&= \int_0^T \frac{1}{2}\sum_k \left[\alpha^2\tilde{c}(\boldsymbol{x}_{m,k},t)^2 - 2\alpha\tilde{c}(\boldsymbol{x}_{m,k},t)\left\{c^n(\boldsymbol{x}_{m,k},t) - M(t)\right\} + B\right] dt,
\end{aligned}$$

  where B represents the terms that do not include α.
- The optimal value of α that minimizes J^{n+1} can then be determined from,

$$\frac{dJ^{n+1}}{d\alpha} = \int_0^T \sum_k \left[\alpha\tilde{c}(\boldsymbol{x}_{m,k},t)^2 - \tilde{c}(\boldsymbol{x}_{m,k},t)E_r^n(\boldsymbol{x}_{m,k},t)\right] dt = 0,$$

  so that

$$\alpha_{optimal} = \frac{\int_0^T \sum_k \tilde{c}(\boldsymbol{x}_{m,k},t)E_r^n(\boldsymbol{x}_{m,k},t)dt}{\int_0^T \sum_k \tilde{c}(\boldsymbol{x}_{m,k},t)^2 dt}. \tag{17}$$

- The scalar source in the next iteration $(n+1)$ is therefore be updated in accordance with Eq. 15 using the optimal value of α from Eq. 17

Appendix B: Sensors Positions

The positions of the source and sensors for all considered cases are listed in this section. The coordinates are expressed in accordance with the setup presented in Section 2 and non-dimensionalized by the half height of the channel h.

Table 1 Source and sensor positions for the case with one sensor

x_s	y_s	z_s
1.0000	1.0000	1.5708
$x_{m,k}$	$y_{m,k}$	$z_{m,k}$
4.0000	1.0000	1.5708
7.0000	1.0000	1.5708
10.0000	1.0000	1.5708
13.0000	1.0000	1.5708

Table 2 Source and sensors positions for the case with multiple sensors. The same sensor pattern was used for both cases with source at $y_s^+ = 10$ and $y_s^+ = 20$

$y_s^+ = 150$			$y_s^+ = 50$			$y_s^+ = 30$			$y_s^+ = 10$ & 20		
x_s	y_s	z_s	x_s	y_s	z_s	x_s	y_s	z_s	x_s	y_s	z_s
1.0	1.0	1.5708	1.0	0.3333	1.5708	1.0	0.2	1.5708	1.0	0.0667	1.5708
									1.0	0.1333	1.5708
$x_{m,k}$	$y_{m,k}$	$z_{m,k}$	$x_{m,k}$	$y_{m,k}$	$z_{m,k}$	$x_{m,k}$	$y_{m,k}$	$z_{m,k}$	$x_{m,k}$	$y_{m,k}$	$z_{m,k}$
13.0	1.0000	1.5708	13.0	0.0667	1.5708	13.0	0.0667	1.5708	13.0	0.0667	1.5708
13.0	1.0000	0.7854	13.0	0.0667	0.7854	13.0	0.0667	0.7854	13.0	0.0667	0.7854
13.0	1.0000	2.3562	13.0	0.0667	2.3562	13.0	0.0667	2.3562	13.0	0.0667	2.3562
13.0	1.5000	1.5708	13.0	0.3333	1.5708	13.0	0.2000	1.5708	13.0	0.5000	1.5708
13.0	1.5000	0.7854	13.0	0.3333	0.7854	13.0	0.2000	0.7854	13.0	0.5000	0.7854
13.0	1.5000	2.3562	13.0	0.3333	2.3562	13.0	0.2000	2.3562	13.0	0.5000	2.3562
13.0	0.5000	1.5708	13.0	0.7333	1.5708	13.0	0.5600	1.5708	13.0	0.2500	1.5708
13.0	0.5000	0.7854	13.0	0.7333	0.7854	13.0	0.5600	0.7854	13.0	0.2500	0.7854
13.0	0.5000	2.3562	13.0	0.7333	2.3562	13.0	0.5600	2.3562	13.0	0.2500	2.3562
13.0	0.7500	1.5708	13.0	0.2001	1.5708	13.0	0.1335	1.5708	13.0	0.1584	1.5708
13.0	0.7500	1.1781	13.0	0.2001	1.1781	13.0	0.1335	1.1781	13.0	0.1584	1.1781
13.0	0.7500	1.9635	13.0	0.2001	1.9635	13.0	0.1335	1.9635	13.0	0.1584	1.9635
13.0	1.2500	1.5708	13.0	0.5335	1.5708	13.0	0.3402	1.5708	13.0	0.3750	1.5708
13.0	1.2500	1.1781	13.0	0.5335	1.1781	13.0	0.3402	1.1781	13.0	0.2500	1.1781
13.0	1.2500	1.9635	13.0	0.5335	1.9635	13.0	0.3402	1.9635	13.0	0.2500	1.9635
13.0	1.0000	1.1781	13.0	0.3333	1.1781	13.0	0.2000	1.1781	13.0	0.0667	1.1781
13.0	1.0000	1.9635	13.0	0.3333	1.9635	13.0	0.2000	1.9635	13.0	0.0667	1.9635

References

1. Saunier, O., Mathieu, A., Didier, D., Tombette, M., Quélo, D., Winiarek, V., Bocquet, M.: An inverse modeling method to assess the source term of the Fukushima nuclear power plant accident using gamma dose rate observations. Atmos. Chem. Phys. **13**(22), 11,403–11,421 (2013)
2. Steinhauser, G., Brandl, A., Johnson, T.E.: Comparison of the chernobyl and fukushima nuclear accidents: a review of the environmental impacts. Sci. Total Environ. **470**, 800–817 (2014)
3. Balkovsky, E., Shraiman, B.I.: Olfactory search at high Reynolds number. Proc. Natl. Acad. Sci. **99**(20), 12,589–12,593 (2002)
4. Ishida, H., Wada, Y., Matsukura, H.: Chemical sensing in robotic applications: A review. IEEE Sensors J. **12**(11), 3163–3173 (2012)
5. Kowadlo, G., Russell, R.A.: Robot odor localization: A taxonomy and survey. Int. J. Robot. Res. **27**(8), 869–894 (2008)
6. Ishida, H., Kagawa, Y., Nakamoto, T., Moriizumi, T.: Odor-source localization in the clean room by an autonomous mobile sensing system. Sensors Actuators B Chem. **33**(1), 115–121 (1996)
7. Ishida, H., Suetsugu, K.i., Nakamoto, T., Moriizumi, T.: Study of autonomous mobile sensing system for localization of odor source using gas sensors and anemometric sensors. Sensors Actuators A Phys. **45**(2), 153–157 (1994)
8. Ferri, G., Caselli, E., Mattoli, V., Mondini, A., Mazzolai, B., Dario, P.: Spiral: A novel biologically-inspired algorithm for gas/odor source localization in an indoor environment with no strong airflow. Robot. Auton. Syst. **57**(4), 393–402 (2009)
9. Li, W., Farrell, J., Pang, S., Arrieta, R.M., et al.: Moth-inspired chemical plume tracing on an autonomous underwater vehicle. IEEE Trans. Robot. **22**(2), 292–307 (2006)
10. Webster, D., Volyanskyy, K., Weissburg, M.: Bioinspired algorithm for autonomous sensor-driven guidance in turbulent chemical plumes. Bioinspir. Biomim. **7**(3), 036,023 (2012)
11. Baklanov, A., Aloyan, A., Mahura, A., Arutyunyan, V., Luzan, P., Campos-Ramos, A.A., Aragon-Pina, A., Alastuey, A., Galindo-Estrada, I., Querol, X., et al.: Atmospheric pollution research. Evaluation **2**(4), 400–529 (2011)
12. Ferri, G., Jakuba, M.V., Mondini, A., Mattoli, V., Mazzolai, B., Yoerger, D.R., Dario, P.: Mapping multiple gas/odor sources in an uncontrolled indoor environment using a Bayesian occupancy grid mapping based method. Robot. Auton. Syst. **59**(11), 988–1000 (2011)
13. Keats, A., Yee, E., Lien, F.S.: Bayesian inference for source determination with applications to a complex urban environment. Atmos. Environ. **41**(3), 465–479 (2007)
14. Marjovi, A., Marques, L.: Optimal swarm formation for odor plume finding. IEEE Trans. Cybern. **44**(12), 2302–2315 (2014)
15. Matthes, J., Groll, L., Keller, H.B.: Source localization by spatially distributed electronic noses for advection and diffusion. IEEE Trans. Signal Process. **53**(5), 1711–1719 (2005)
16. Tsukahara, T., Oyagi, K., Kawaguchi, Y.: Estimation method to identify scalar point source in turbulent flow based on Taylor's diffusion theory. Environ. Fluid Mech. **16**(3), 521–537 (2016)
17. Vergassola, M., Villermaux, E., Shraiman, B.I.: 'infotaxis' as a strategy for searching without gradients. Nature **445**(7126), 406–409 (2007)
18. Barbieri, C., Cocco, S., Monasson, R.: On the trajectories and performance of infotaxis, an information-based greedy search algorithm. EPL (Europhysics Letters) **94**(2), 20,005 (2011)
19. Voges, N., Chaffiol, A., Lucas, P., Martinez, D.: Reactive searching and infotaxis in odor source localization. PLoS Comput. Biol. **10**(10), e1003,861 (2014)
20. Iwamoto, K., Suzuki, Y., Kasagi, N.: Database of fully developed channel flow. Department of Mechanical Engineering, The University of Tokyo, THTLAB Internal Report No. ILR-0201 (2002)
21. Hasegawa, Y., Kasagi, N.: Dissimilar control of momentum and heat transfer in a fully developed turbulent channel flow. J. Fluid Mech. **683**, 57–93 (2011)
22. Zaki, T.A., Saha, S.: On shear sheltering and the structure of vortical modes in single-and two-fluid boundary layers. J. Fluid Mech. **626**, 111–147 (2009)
23. Hasegawa, Y., Kasagi, N.: Low-pass filtering effects of viscous sublayer on high Schmidt number mass transfer close to a solid wall. Int. J. Heat Fluid Flow **30**(3), 525–533 (2009)